Experiments in Fluids 31 (2001) 153–161 © Springer-Verlag 2001

Frequency analysis of turbulent compressible flows by laser vibrometry

N. Mayrhofer, J. Woisetschläger

Abstract The objective of this work was the application of laser vibrometry as a tool for non-intrusive measurement of frequency spectra in turbulent flows. A laser vibrometer system together with a signal analyser was used to obtain frequency spectra of density fluctuations across a turbulent free jet. Since laser vibrometry is based on interferometric techniques, the derived signals are path integrals along the measurement beam. Frequency spectra recorded in the rotational symmetric flow were then treated using Abel inversion in order to derive information on local density fluctuations. Results for two different flow conditions were compared to spectral data from a constant temperature anemometer and a pitot-mounted pressure sensor.

List of symbols

$D(r)$	radially symmetric distribution
f	frequency
G	Gladstone–Dale constant
$I(x)$	integral data
j	imaginary unit
l	number of independent events or structures
M	number of samples in time
n	refractive index
p	pressure
r	radial coordinate
R	inner pipe radius
$S_{\varphi'}(f)$	power spectral density of phase fluctuation $\varphi'(t)$
$S_{\rho'}(f)$	power spectral density of density fluctuation $\rho'(t)$
SNR	signal to noise ratio
t	time
v	velocity
x	coordinate in horizontal traversing direction, perpendicular to the wave front propagation z
y	coordinate in direction of jet axis and perpendicular to x
z	coordinate in the direction of the wave front propagation

Greek letters

φ	phase of the object wave front relative to the reference wave
Φ	Fourier transform of φ with respect to t
λ	wavelength of laser light
λ_0	vacuum wavelength of laser light
ρ	density
P	Fourier transform of ρ with respect to t
σ	standard deviation of a set of data

Indices

i	index of gas component
k	frequency index
m	time index

Superscripts

$\bar{}$	mean value
$'$	fluctuating component

Received: 21 February 2000/Accepted: 13 December 2000

N. Mayrhofer, J. Woisetschläger (✉)
Institute for Thermal Turbomachinery and Machine Dynamics
Graz University of Technology, Inffeldgasse 25, 8010 Graz
Austria
e-mail: ttm@ttm.tu-graz.ac.at
Tel.: +43-316-8737226; Fax: +43-316-8737234
url: http://ttm.tu-graz.ac.at

This work was supported by the Austrian Science Foundation (FWF) and the Austrian Ministry for Science and Traffic and was part of the awarded grant Y57-EC (Non-intrusive measurement of turbulence in turbomachinery, J. Woisetschläger).
We would also like to acknowledge Drs. Lewin and Siegmund from Polytec for their assistance with regards to the electronic data processing within the vibrometer systems.

1 Introduction

The Institute for Thermal Turbomachinery and Machine Dynamics focuses on flows in modern and future turbomachinery which are characterised by high inlet temperatures (as high as 1400 °C and above), subsonic and transonic regions in a compressible medium of gas or steam. On one side these flows are highly turbulent and unsteady while on the other the flow next to the surface may be either laminar or turbulent. Several authors have suggested experiments to find starting points for the improvement of turbulent flow modelling in turbomachinery (see e.g. Mayle 1991; Mayle et al. 1998; Gostelow et al. 1996, 1997). Among those experiments are the measurements of turbulence intensities and spectrum characteristics in the gas path, together with the experimental investigation of transition at high free-stream turbulence, as well as wake-induced transition and boundary-layer separation. The use of constant temperature anemometry and time-resolved pressure recordings is frequently not possible with these types of transonic, compressible flows at high temperature.

On the other hand, interferometric methods are well established in vibration analysis, where interferometers

enable frequency and modal analysis. This paper focuses on the applicability of a well-established interferometric technique – known as laser vibrometry – for frequency analysis in compressible flows.

In a first test, a circular free jet was investigated due to its easy operability and well-known behaviour.

2 Background

2.1 Basic principle

Interferometric determination of density is based on the relation between density and refractive index. A commonly used description is the Gladstone–Dale relation

$$(n-1)_{\lambda,\rho} = G_\lambda \rho = \sum_i G_{\lambda,i}\rho_i \qquad (1)$$

(e.g. Merzkirch 1987), where G denotes the Gladstone–Dale constant for a mixture of gases, G_i being for a component, ρ the density of the fluid and ρ_i the partial density of the ith component respectively. Density changes in compressible flows thus manifest in changes of refractive index, which delay a light wave while propagating through this compressible fluid. The equation

$$\varphi(x,y,t) = \frac{2\pi}{\lambda_0}\int_{\text{object}} n(x,y,z,t)\,\mathrm{d}z - \frac{2\pi}{\lambda_0}\int_{\text{reference}} n(x,y,z)\,\mathrm{d}z \qquad (2)$$

describes the path integrating nature of interferometric measurements, which means that a delay in phase in any point along the optical path of the light contributes to an integral phase change (denoted by "object" in Eq. 2). This phase change is then detected by superposition of this object light wave with a reference light wave of constant phase. Changes in density thus produce interferometric fringe movement. $\varphi(x,y,t)$ is the phase of the object light wave relative to the constant reference wave at the detector. $n(x,y,z,t)$ is the refractive index of the object field under observation at the time t, $n(x,y,z)$ the refractive index in the reference path.

It should be mentioned that techniques using light deflections, depending on spatial gradients in a refractive index field are used for flow-field visualisation (shadow and Schlieren techniques) and also for frequency analysis of density fluctuations (Heinemann et al. 1976; Garg and Settles 1998; Merzkirch 1987). In contrast, the technique described in this paper is sensitive to the phase change of the light wave due to density changes in the compressible fluid and does not need light deflection effects.

2.2 Principle of operation

2.2.1 Detecting vibration

Interferometric techniques are widely used for vibration analysis of different types of machinery. Usually a frequency analysis of surface vibration at one position is followed by a modal analysis using scanning devices, digital holographic interferometry, electronic speckle interferometry, or similar (e.g. Brown et al. 1999). For continuous detection of surface vibration a Michelson or Mach–Zehnder type interferometer incorporating an open air path can be used (Lewin et al. 1990; Lewin 1999).

Figure 1 shows the principle optical set-up of such an interferometer, commonly called a "single-point vibrometer", used in the work presented here. The laser beam is split into object and reference beam running along different paths, with both beams interfering at the position of the detector.

Keeping the refractive index constant, Eq. (2) reduces to

$$\varphi(t) = \frac{4\pi}{\lambda} z(t) \qquad (3)$$

with λ equal λ_0/n.

Here, a change in the phase of the light wave $\varphi(t)$ in the open air path of the system (one arm of the interferometer) is caused by vibration of the surface, back-scattering the laser beam. $z(t)$ is the object's surface position.

Figure 2 shows the principle electronic modules within the vibrometer system for decoding displacement and velocity of an object from the detector signal (see Selbach et al. 1992). A master oscillator is driving a Bragg cell in the reference path of the vibrometer to overcome sign ambiguity (not shown in Fig. 1). For the velocity output (decoding the Doppler frequency of the detector signal) a local oscillator locked into the signal of this master oscillator is used to mix the detector signals of smaller bandwidth down into a base band where they are demodulated more accurately. Different FM-demodulation principles are offered depending on the application. Contrary, displacement decoding is based on fringe counting.

2.2.2 Detecting density fluctuations

When keeping the geometrical path constant and using Eq. (1) to substitute the refractive index $(n-1)$ by the density ρ, Eq. (2) reduces to

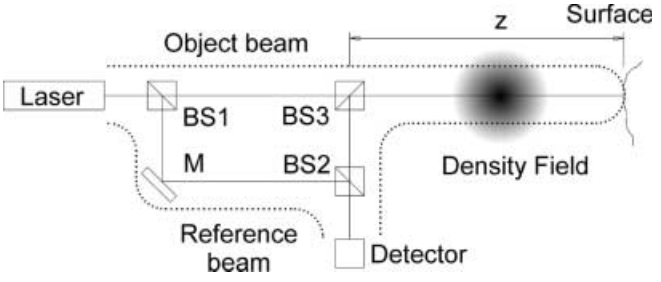

Fig. 1. The principles of a laser vibrometer. The laser beam is split into object and reference beam in a Mach–Zehnder interferometer. While the reference beam remains inside the device itself, the object beam leaves the vibrometer at beam-splitter 3 (BS3) and re-enters after reflection from an object's surface to interfere with the reference beam. The dotted lines indicate the integration paths

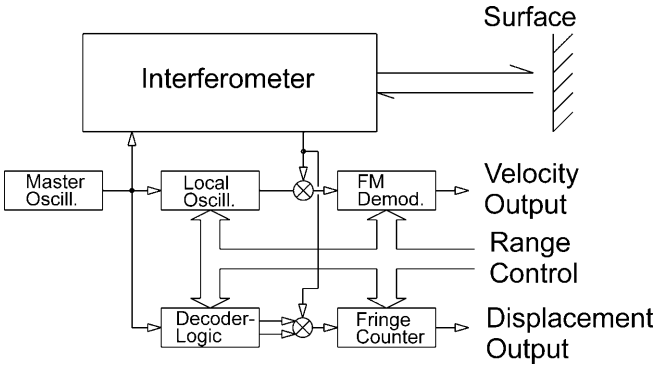

Fig. 2. Principal signal paths inside the vibrometer system. The master oscillator drives a Bragg cell in the reference beam introducing a frequency shift that distinguishes the displacement direction. The local oscillator generates a signal at a fraction of the master oscillators frequency for down mixing of detector signals. The final FM demodulation gives a signal proportional to the velocity. Displacement measurement is based on fringe counting after a phase multiplier for better resolution (Selbach et al. 1992)

$$\varphi(t) = \frac{4\pi}{\lambda_0} G \int_{z_0}^{z_1} \Delta\rho \; \mathrm{d}z \tag{4}$$

presenting the sensitivity to density changes of the type of interferometer shown in Fig. 1. With respect to the decomposition into mean and fluctuating terms in fluid dynamics, $\Delta\rho$ can be substituted by

$$\begin{aligned} \Delta\rho(z,t) &= \rho_{\text{object}}(z,t) - \rho_{\text{reference}} \\ &= \overline{\rho(z)} + \rho'(z,t) - \rho_{\text{reference}}, \end{aligned} \tag{5}$$

where $\overline{\rho(z)}$ is the long-time average of density in the object field, $\rho'(z,t)$ the fluctuating density component in the object field containing the information on flow turbulence, $\rho_{\text{reference}}$ the (constant) density in the reference light path within the vibrometer device.

While in most vibrometer applications on machinery the phase shift contribution given by Eq. (3) exceeds the contribution by Eq. (4) significantly, in certain types of fluid flow it will be the opposite way. This is always the case when significant density changes take place in the flow (e.g. in compressible high speed flows with pronounced pressure gradients, temperature or concentration fluctuations) especially in the high frequency range, where machine oscillations are usually of small amplitude.

Separation of the two effects is principally not possible without additional information. In the frequency domain however, separation may be possible if both effects take place in different frequency bands.

2.3 Frequency analysis

According to Eq. (4) a stationary turbulent compressible flow investigated by the interferometer gives a broadband random signal $\varphi(t)$. The spectrum of such a random signal is continuously distributed over frequency while its shape depends on the type of compressible flow and is discussed in numerous publications (for frequency spectra see e.g. McComb 1990; Romano 1995). According to Eqs. (4) and (5), $\varphi(t)$ can be also separated into a long-term average expression $\overline{\varphi}$ and a fluctuating phase component $\varphi'(t)$.

Frequency analysis is used for statistical description of random signals even if they are not periodic. Making use of the Fourier transform we can define the optical phase fluctuations in the frequency domain $\Phi'(f)$ by

$$\Phi'(f) = \int_{-\infty}^{\infty} \varphi'(t) \mathrm{e}^{-j2\pi ft} \; \mathrm{d}t. \tag{6}$$

As Eq. (6) is not a function of time it is possible to reproduce the description of a turbulent flow in terms of amplitude and phase spectra.

In practice the discrete description

$$\Phi'(f_k) = \frac{1}{M} \sum_m \varphi'(t_m) \mathrm{e}^{-j2\pi f k t_m} \tag{7}$$

is used instead with k the index of frequency, m the index of the time domain and M the number of samples in time (Newland 1975). Depending on the measurement time in relation to the time scale of the flow, an acceptable approximation of the spectrum in Eq. (6) by Eq. (7) can be obtained by ensemble averaging over numerous spectra. For practical applications, however, the need for a long measurement time naturally collides with other interests.

Investigating stationary turbulent flows of compressible fluids, the frequency analysis of the interferometer signal provides the constant DC signal caused by the density signals $\overline{\rho(z)}$ and $\rho_{\text{reference}}$ in Eq. (5), as well as the AC signal from $\rho'(z,t)$. This fluctuating density part $\rho'(z,t)$ can be presented by $\mathrm{P}'(z,f)$ in the Fourier domain. $\Phi'(f)$ now is the Fourier transform of the AC signal $\varphi'(t)$ related to $\rho'(z,t)$. Thus, the fluctuating component in Eq. (4) is transformed into

$$\Phi'(f) = \frac{4\pi}{\lambda_0} G \int_{z_0}^{z_1} \mathrm{P}'(z,f) \mathrm{d}z \tag{8}$$

by Eq. (6) with $\Phi'(f)$ and $\mathrm{P}'(z,f)$ being complex functions.

Measurement of absolute density using the DC components of the signal is hardly possible due to limited long time stability of the vibrometer's displacement signal as well as inevitable stochastic changes in path length, especially when traversing has to be done. Other interferometric methods are available for this purpose (e.g. Merzkirch 1987; Oertel and Oertel 1989).

The complex spectrum $\Phi'(z,f)$ can be represented by its magnitude and phase spectrum, or by its real and imaginary part. The phase spectrum of such a single signal, however, will be quite random and only of interest when set in relation to a reference measurement carried out at the same time (Randall and Tech 1977; Romano 1995). By doing so, coherent structures like acoustic waves can be identified by their signal phase patterns. Therefore we used a second vibrometer, but any other device capable of the same bandwidth, e.g. constant temperature anemometer or fast pressure measurement, could also have been used here.

The spectral power density $S_{\rho'}(f)$, used finally for the presentation of results, can be calculated from the peak amplitude spectrum as

$$S_{\rho'}(f) = \frac{|\mathrm{P}'(f)|^2}{2\Delta f} \quad \text{for} \quad f > 0 \tag{9}$$

assuming uniform distribution of power within the discrete frequency bins of frequency width Δf (frequency resolution).

2.4 Abel inversion

For testing purposes, we used a free jet of cylindrical symmetry. Inside a turbulent flow, however, the density distribution $\rho(x,y,z,t)$ is stochastic and thus non-symmetric. Making use of the Fourier transform (Eq. 6 above) the frequency representation $\mathrm{P}'(x,y,z,f)$ of the density fluctuations was used. The main advantage of this Fourier transform is the formal re-establishment of symmetry that is lost by the stochastic nature of turbulence in the time domain.

In the present experiment, cylindrical symmetry was not only assumed for the long time averages such as density field $\overline{\Delta\rho(x,y,z)}$, but also for the Fourier spectrum $\mathrm{P}'(x,y,z,f)$.

To obtain local information from integral interferometric measurements, reconstruction algorithms usually used in computerised tomography are applied, based on multi-directional observation of the object (e.g. Vest 1989; Vukičević et al. 1990; Kreis 1996). In the special case, when a distribution proves to be rotationally symmetric, the Abel inversion (or inverse Abel transform)

$$D(r) = -\frac{1}{\pi}\int_{r}^{r_\infty} \frac{\mathrm{d}I(x)}{\mathrm{d}x}\frac{1}{\sqrt{x^2 - r^2}}\mathrm{d}x \tag{10}$$

can be used. This inversion provides a radially symmetric distribution $D(r)$ from a set of integral data $I(x)$ along the direction of beam propagation z, recorded by traversing a line (x direction) orthogonal to z.

Usually the projection data $I(x)$ are not given analytically but as a set of discrete measurement data. Different numerical schemes have been presented and compared in Pretzler et al. (1992). We used a standard f interpolation scheme as well as an inversion based on the Backus–Gilbert algorithms (Backus and Gilbert 1970).

The f interpolation divides the radial distribution into rings of equal density, where each ring is fitted by a third-order polynomial for inversion. As the calculation proceeds from the periphery to the centre, all contributions of outer rings can be computed and the contribution of the inner next ring fitted to the measured data points $I(x)$. In addition to this least-squares criterion, smoothing must be provided by forcing neighbouring polynomials to overlap. There is always concurrence between effective smoothing and the deviation of the calculated integral from the measured data. By gradually working from the outer regions to the centre, calculation and measurement errors also increase in the centre region.

Being aware of this problem, a linear combination of a so-called "resolution functional" and a "stabilising functional" is used in the Backus–Gilbert algorithm. The weighting of both criteria can be given with a single input value called a "trade-off parameter". With this method, the algorithm is used to find a smooth curve with a small deviation of the measured data and the integral from the calculated data.

For the procedures described above a software package was used, which was developed at Graz University of Technology and is readily available on the Internet's public domain (Hipp et al. 1999).

As the available algorithms are written for scalar input only, the real and imaginary parts of the integral function $\Phi'(x,f)$ can be Abel inverted separately thus leading to real and imaginary parts of local $\mathrm{P}'(r,f)$ for each frequency f repeatedly. In case the complex function $\Phi'(x,f)$ does not contain a strong influence of phase, e.g. the phase spectrum close to zero, the magnitude $|\Phi'(x,f)|$ can be used for Abel inversion to obtain local $|\mathrm{P}'(r,f)|$. The separate inversion of real and imaginary parts introduces more noise into the results than a direct inversion of the magnitude. The procedure was tested by the Abel transform of simulated concentric waves and inversion of the resulting distribution for magnitude and phase.

3 Experimental set-up

3.1 Arrangement and techniques

For our tests we used a fully developed turbulent free jet. The overall design is shown in Fig. 3. The jet emerged from a brass pipe with an inner tube diameter of 22.0 mm, an outer tube diameter of 24.0 mm and a length of 585 mm, with five wire screens of 0.5 mm grid size at its lower end, 560 mm from the circular orifice and 5 mm spacing between them. The jet was isothermal with a temperature of 20 °C. The velocity of 73 m/s at the centre was measured using a Prandtl tube. The average velocity calculated from the velocity profile was 67 m/s, the mass flow was 106 kg/h and the Reynolds number with respect to the inner diameter was about 94,000.

Two different set-ups were used. In the first set-up, the pipe was fed by pressurised air via a settling chamber (200 mm high with a 200 mm diameter), where total pressure and temperature had been measured. This settling chamber consisted of a radial diffuser, a fibrous mat and a radially symmetric nozzle serving as a pipe inlet. This set-up produced a uniform and smooth jet flow, while in the second set-up a rubber hose of 1 m length and 20 mm i.d. connected the brass pipe with a much simpler settling chamber (500 mm long, 100 mm high and 100 mm wide). In this second set-up strong acoustic waves were produced, mainly by the plug-in connectors in the rubber hose that had an i.d. of 6 mm and thus forcing critical flow. These acoustic waves manifested themselves in the jet emerging from the pipe.

Two Polytec laser vibrometers OFV-353 with an OFV-3001 controller were used, with an OVD-02 velocity decoder and an OVD-20 displacement decoder in one

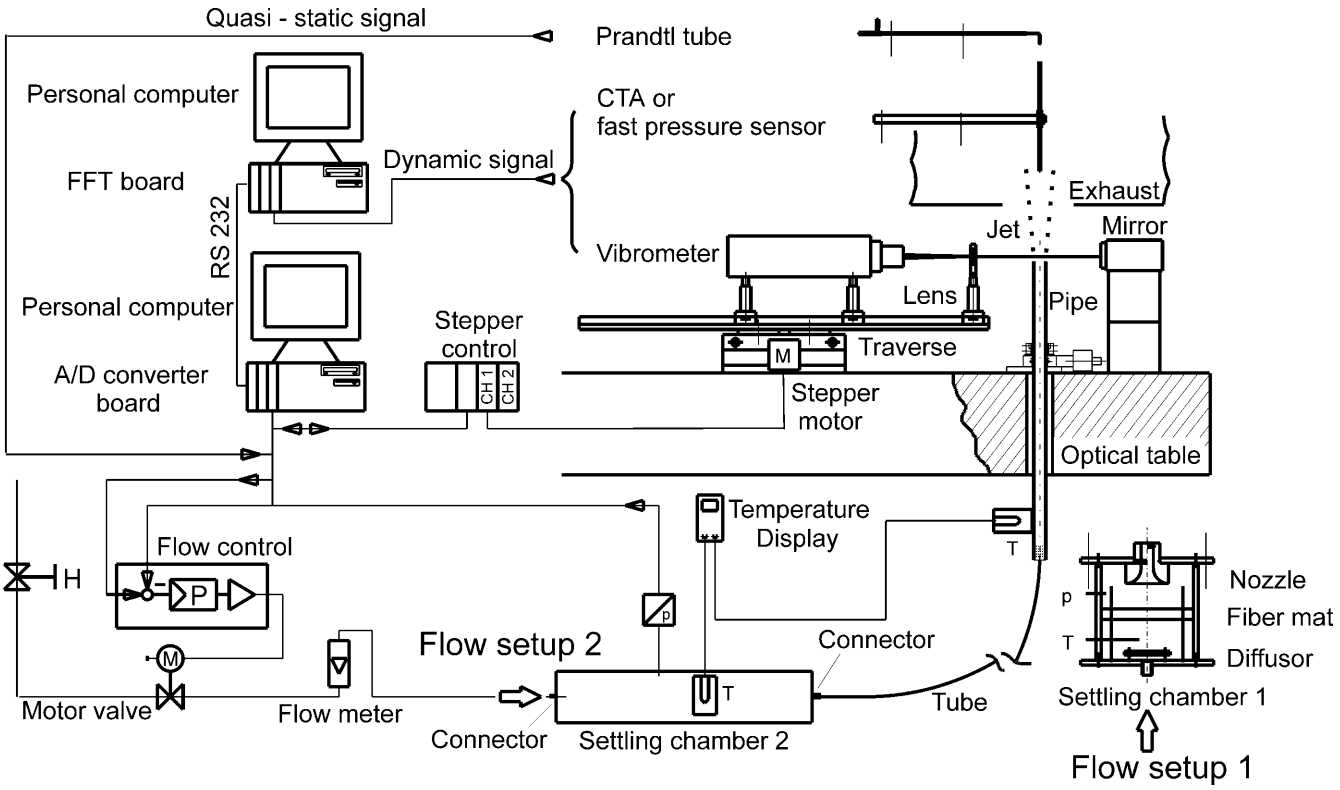

Fig. 3. Experimental set-up for the recording of frequency spectra in a free concentric jet by laser vibrometry, constant temperature anemometry (CTA) and a fast pressure sensor. Two flow set-ups were used, one (set-up 1) without and one (set-up 2) with the generation of strong acoustic waves in the flow

of them. The main systems had a mid-range objective with a 7 mm aperture. While the velocity decoder provided four ranges from 5 to 1000 mm/sV with a resolution of approximately 0.5 μm/s and a frequency bandwidth of 250 kHz in the 5 mm/sV range (this range was used for the measurements described in the following chapters), the displacement decoder had eight ranges starting with 2, 8 and 32 nm resolution per digit and frequency ranges of 25 and 75 kHz in these high resolution modes.

The measurement of density fluctuations was carried out using a nearly parallel laser beam of approximately 1.5 mm diameter, produced by means of a slightly inclined lens (focus = −40 mm) introduced into the focused beam of the vibrometer. The beam was reflected by a mirror so that it passed the measuring volume twice and was reflected back into the aperture of the system. The mirror was glued on a mount of approximately 5 kg mass, so that problems with cross-sensitivity against vibration of the mirror were reduced.

To reference the phase fluctuations of the signal as explained before, a second Polytec laser vibrometer type OFV-303 with OFV-3001 controller and OVD-02 velocity decoder (not shown in Fig. 3) was used for some measurements.

For purposes of comparison, pressure and velocity measurements were also carried out for the same positions as scanned by the laser beam. The velocity measurements were done with a single channel constant temperature anemometer (CTA). We used a 55D01 controller with a one-dimensional DISA 55P11 probe calibrated by reference recordings from a Prandtl tube PBA-12-F-11-K from United Sensor. For the measurement of the pressure fluctuations we used a miniaturised Entran EPI-411–3.5B sensor with 3.5 bar range and 2 mm sensitive cross-section. Due to its relatively large size we also tried to use an oil-filled conical sensor tap providing a higher spatial resolution but this tap acted as a low-pass filter to the pressure fluctuations within the observed bandwidth and therefore was not used for the comparison.

3.2
Data acquisition and control

The signals from laser vibrometers, CTA and pressure sensor were fed into a National Instruments NI4551 Dynamic Signal Analyser board capable of online fast Fourier transform (FFT) of two channels with 95 kHz bandwidth each, mounted in a personal computer. Data recording and evaluation was performed by programs developed with National Instruments LabVIEW software.

This computer was master to a second one controlling a stepper motor traverse which was used to position the different measurement tools within the free jet region in steps of 0.5 mm. Additionally, the slave computer provided a reference voltage to a flow-control unit and was used to sample control data on pressure. Based on the pressure recordings in the settling chamber, this unit was acting on a valve in the air supply keeping the air flow constant. The pressure in the settling chamber was controlled to the desired value at an error of approximately ±5 mbar. For each sampled position a linear rms average

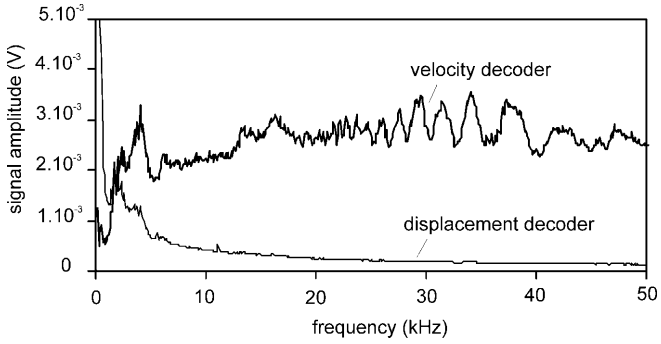

Fig. 4. Comparison of the frequency spectra recorded by the laser vibrometer using the Polytec OVD-02 velocity decoder and OVD-20 displacement decoder for position 0 mm in Fig. 5b. While the velocity decoder provided the temporal derivative of the phase fluctuations for subsequent Fourier analysis, the displacement decoder gave the phase fluctuations directly, but at a significantly less signal to noise ratio and smaller bandwidth. The noise for both detectors is about 100 μV

of up to 8,000 FFTs was used for analysis, with a sampling rate of 204.8 kHz and 2,048 values for each FFT scan (providing 100 Hz resolution in the resulting frequency plots). Having a recording time of 2 min for each position and a short settling after each traverse movement, these measurements took up to 7 h for each traversed line. From these data an error estimate of 1% results for $S_{\varphi'}$.

4 Results

4.1 Frequency spectra recorded by laser vibrometer

Figure 4 shows the spectrum for the temporal derivative of the interferometric phase fluctuations $\partial/\partial t\Phi'(x,f)$ recorded from the velocity decoder and the spectrum for the interferometric phase fluctuations $\Phi'(x,f)$ received from the displacement decoder (direct $\Phi'(x,f)$ signal) for position 0 mm in flow set-up 2. The signal to noise ratio (SNR) was from 15 to 30 for the velocity decoder in the 5–50 kHz range compared to less than 4 for the displacement decoder in the same range. Additionally the displacement decoder in the 0.5 μm/V range is limited to the 25 kHz bandwidth only. For that reason the velocity decoders from the vibrometer systems were used for measurements.

For further evaluation the temporal derivative of the phase fluctuations $\partial/\partial t\Phi'(x,f)$ recorded by the velocity decoder were integrated by

$$\Phi'(x,f) = \frac{1}{2j\pi f}\frac{\partial}{\partial t}\Phi'(x,f) \qquad (11)$$

in order to receive the fluctuation amplitude $\Phi'(x,f)$.

For the flow set-ups in Fig. 3, frequency spectra were recorded, when traversed across the pipe at a height $y = 10$ mm above the orifice. The flow axis is at position $x = 0$ mm and the inner pipe radius is ±11 mm. For each traversed position, one frequency spectrum similar to the one in Fig. 4 was recorded and was plotted in Fig. 5 according to its position. Measurement resolution was 0.5 mm for position and 100 Hz for frequency. These measurement data were smoothed by a relaxation algorithm to reduce noise and were then presented in Fig. 5.

Figure 5a shows a very uniform distribution of integral density fluctuations over frequency for the flow set-up 1 in Fig. 3 (set-up including the settling chamber to suppress acoustic waves). In Figs. 5a and b, the magnitude of $\partial/\partial t\Phi'(x,f)$ is presented. In contrast to Fig. 5a, Fig. 5b gives the fluctuations for the jet in which strong acoustic waves were present (flow set-up 2 in Fig. 3). In addition to shedding vortices, acoustic waves manifest in the interferometric signal by their density changes. The fall-off at constant frequency towards the sides of the jet is much flatter due to the propagation of the waves into the surrounding air. Data were collected for positions –50 mm to 50 mm (twice the span shown in Fig. 5b).

4.2 Interferometric spectra vs. spectra recorded by CTA and the pressure sensor

To compare interferometric data to local data recorded by CTA or pressure probes, Abel inversion of interferometric data was performed to obtain local information on density fluctuations $P'(r,f)$ (see Eq. 10 above). This means that the frequency spectra of the $\partial/\partial t\Phi'(x,f)$ were integrated by Eq. (11) and each set of $\Phi'(x,f = \text{constant})$ was fed to

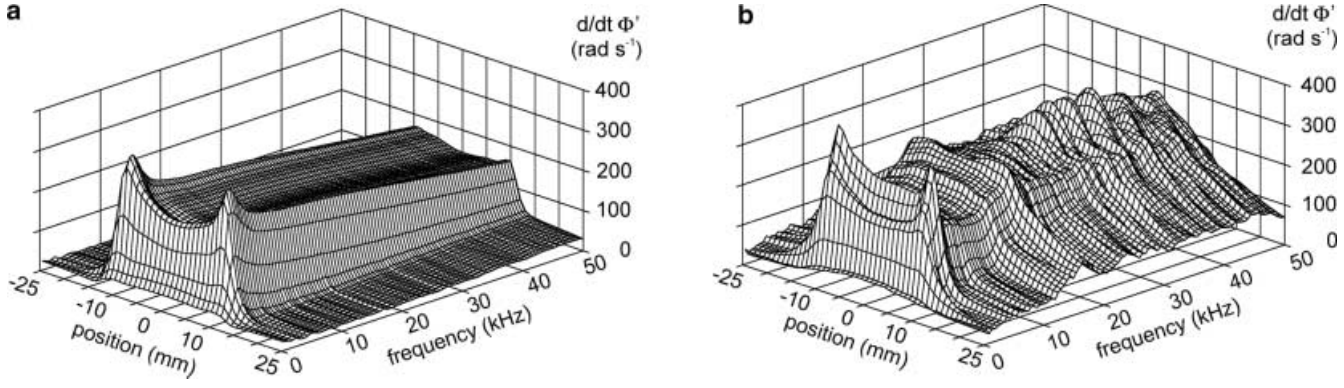

Fig. 5a, b. Frequency plots of the interferometrically-determined fluctuations of phase shift in a round jet **a** without and **b** with strong acoustic waves present. In **a** and **b** the vibrometer was traversed along a line 10 mm above the circular orifice in steps of 0.5 mm. The flow axis was at 0 mm; the pipe radius was at ±11 mm

the Abel-inversion algorithm to obtain the local density fluctuations $P'(r, f = \text{constant})$. Data could be processed as file pools, which eased their handling. The results of Abel inversion of these integral data using the Backus–Gilbert method are given in Figs. 6a–c, again for all frequencies evaluated by the procedure described above.

Figure 6a shows the local data obtained by Abel inversion of the recordings presented in Fig. 5a (set-up 1, flow without strong acoustic waves); Fig. 6b shows the data after inversion of Fig. 5b (flow set-up 2, with strong acoustic waves present). In both cases only the magnitude spectrum of $\Phi'(x, f)$ had been used for inversion. In the case of the flow set-up 1 without acoustic wave generation, this was justified by a close to zero signal phase spectrum of $\Phi'(x, f)$. For the data with strong acoustic waves present, the contribution by the signal phase spectrum made a large difference. Therefore, in Fig. 6c the complex data were used for inversion of both real and imaginary parts and subsequent calculation of the spectral power density (see Eq. 9). In order to demonstrate this impact of signal phase spectrum both Figs. 6b and c had been added. In Fig. 6c the additional noise introduced by the separate inversion of real and imaginary parts of $\Phi'(x, f)$ mentioned at the end of Sect. 2.4 can be clearly observed.

Additionally, spectral plots of the velocity and pressure fluctuations had been recorded using a tangentially orientated CTA (Fig. 6d) and a pressure sensor (Fig. 6e). Both cases were measurements of flow set-up 2 (strong acoustic waves present). These acoustic waves were not observed in the frequency spectrum of velocity recorded by the CTA. On the other hand, these acoustic structures very clearly appeared in the pressure recordings. The measurements by the miniature pressure sensor suffered from a lateral smearing due to the relatively large diameter of the pressure detector (2 mm). In the CTA recording, a vibration mode of the CTA wire at about 35 kHz was visible in the region of the flow while electronic noise shows up outside where measured amplitudes are low. These local data now enable comparison with the interferometrically-derived local density fluctuations.

5 Discussion

Figures 7 and 8 show a comparison of unsmoothed data out of CTA measurements (Figs. 7a, 8a) and Abel-inverted vibrometer measurements (Figs. 7b, 8b) at three different radial positions and three different frequencies. For comparison in Fig. 7 the –5/3 decay according to Kolmogorov is plotted. Besides the spectrum at the flow centre ($r/R = 0$), one in the region of the mixing layer above the pipe wall ($r/R = 1$) and one in the outer region ($r/R = 1.5$) are shown.

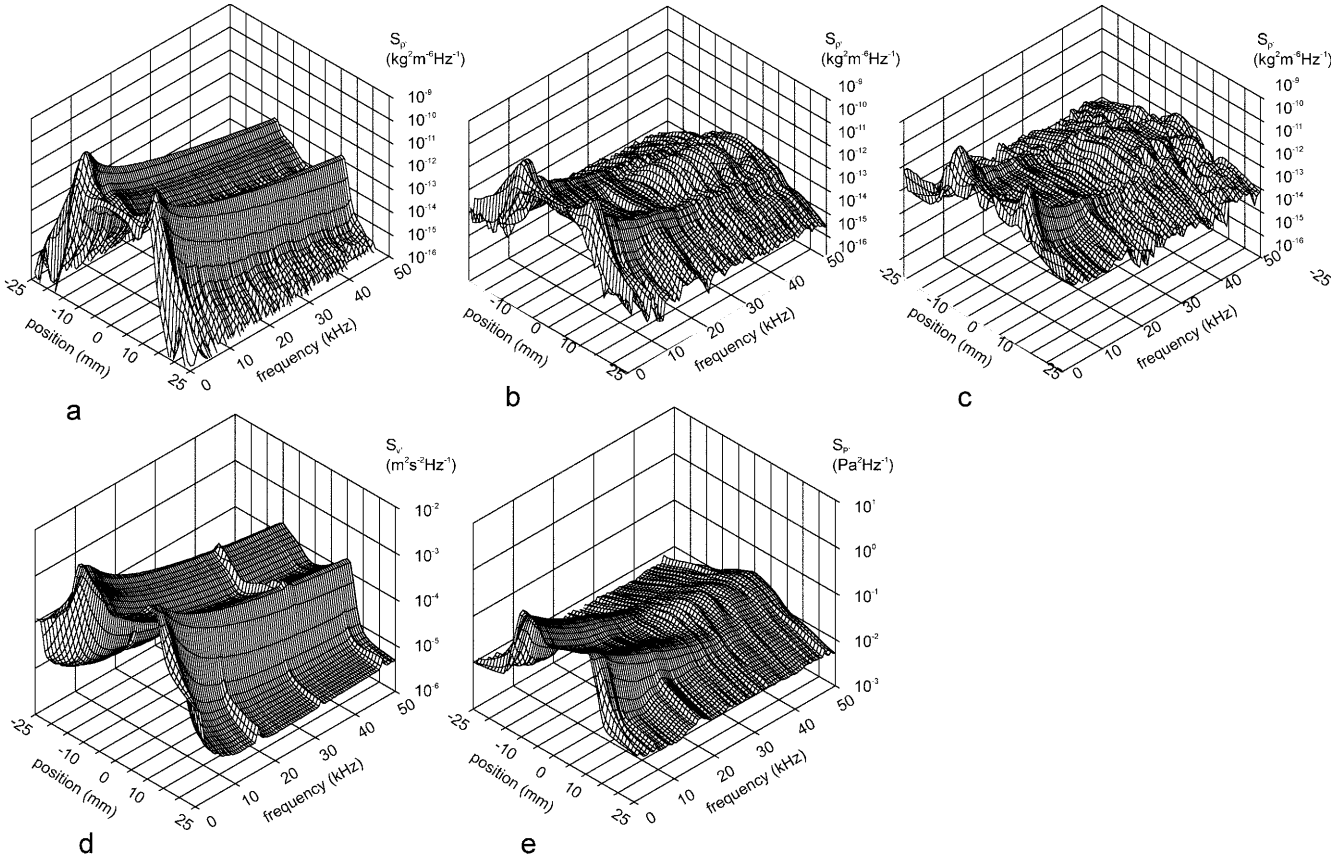

Fig. 6. Comparison of local density fluctuations obtained by interferometry (**a**, **b**, **c**) to local velocity fluctuations recorded by CTA (**d**) and pressure data recorded by a pressure sensor (**e**). In **a**, the flow without the generation of acoustic waves (flow set-up 1 in Fig. 3) and in **b**, **c**, **d** and **e**, the flow with acoustic wave generation are shown (flow set-up 2 in Fig. 3). In **a** and **b** only the signal magnitude was used for Abel inversion of the interferometric data; in **c**, both real and imaginary parts. The flow axis was at 0 mm; the pipe radius was at ±11 mm

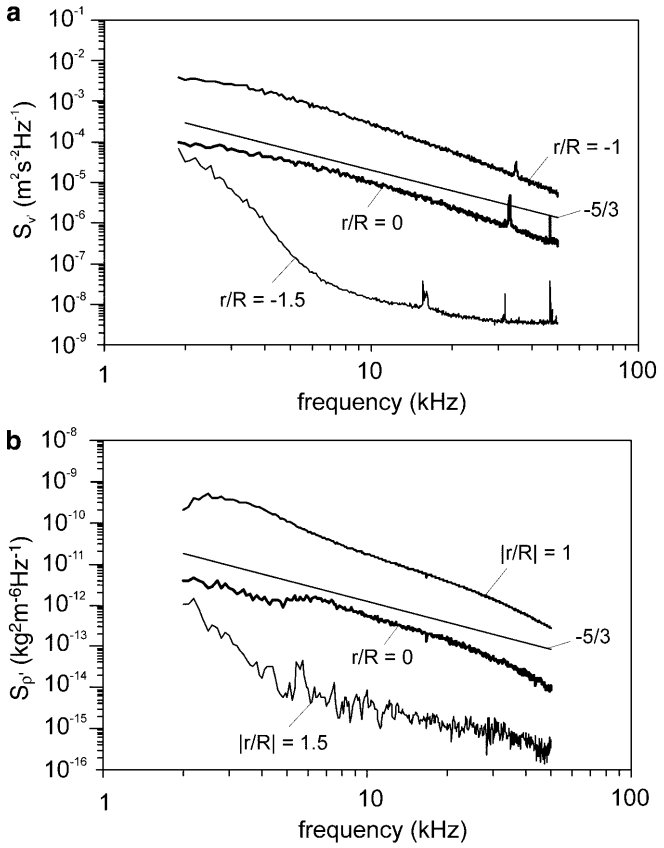

Fig. 7. Comparison of **a** power density spectra for the CTA and **b** the density fluctuations obtained by the laser vibrometer after inversion of these interferometric data to get local information on the density fluctuations for three different radial positions in the centre, in the mixing layer and in the outer region of the flow. The frequency decay along the flow axis is compared to the Kolmogorov –5/3 spectrum (the density was recorded by set-up 1 in Fig. 1, no acoustic waves were generated, see Fig. 6a; for the CTA recording see also Fig. 6d)

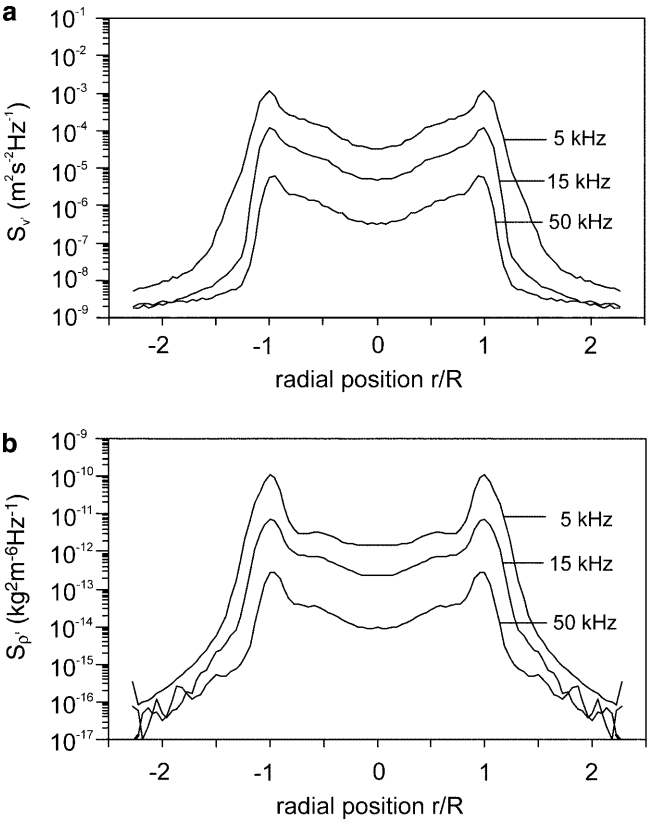

Fig. 8. Comparison of the **a** velocity and **b** density fluctuation profiles at frequencies of 5, 15 and 50 kHz (same flow conditions as in Fig. 7)

Compared to the CTA spectrum (Fig. 7a), the interferometrically-determined density-fluctuation spectrum (Fig. 7b) showed a slightly different behaviour in some parts of the spectra, especially in the outermost region of the mixing layer ($r/R = 1.5$), where the SNR of the density fluctuation signal was small due to its low amplitudes. Therefore, these regions suffered most during the Abel-inversion process since this technique uses integral information all over the diameter to reconstruct these outer areas. Here the limits of detection and reconstruction were reached. Also, in the region below 3 kHz, the temporal derivatives of the density fluctuation were picked up by the velocity decoder, again with smaller SNR compared to the rest of the frequency range.

A slightly stronger decay in the density fluctuations was visible in the high frequency range above 40 kHz, which might be caused by an averaging effect expressed by the path integrating nature of Eq. (4). In the case of two or more uncorrelated flow structures along the beam of light (random fluctuations of density), the interferometer averages on these structures as independent events, thus leading to a decrease in the standard deviation σ by

$$\sigma^2_{\text{mean}} = \frac{\sigma^2}{l} \tag{12}$$

with l being the number of independent events or structures (see e.g. Edwards 1994). For this reason a few large turbulent structures in compressible flows will be present in interferometric measurements, whereas a high number of small structures more or less averages out which is the case especially at high frequencies caused by small turbulent structures.

In Fig. 7a, a vibration of CTA wire is recorded at 30–35 kHz while at approximately 15 and 47 kHz electronic noise can be observed (see also Fig. 6c above).

The power density spectra in Fig. 7 also enabled an estimation of the turbulence level by integration. For the velocity spectra, the data were in accordance with the directly-measured turbulence levels of velocity (3% turbulence level in the centre and 44% turbulence level in the mixing layer at $r/R = \pm 1$). Here, the turbulence level is the fluctuation amplitude with respect to the local mean value. For the density, a 1.7% turbulence level in the centre and 5% turbulence level in the mixing layer resulted from the spectra.

Also the comparison of the velocity and density fluctuations at three frequencies showed similar tendencies (see Fig. 8). While in the mixing layer at $r/R = \pm 1$ the dynamic range of the density fluctuations was slightly larger than that of the velocity, the shape of fluctuations in the core of the flow is nearly identical.

6 Summary

In this paper we applied the technique of laser vibrometry to record frequency spectra of density fluctuations and compared them to spectra recorded with standard techniques for experimental flow investigation as far as possible. In this way spectral maps of density fluctuations were obtained. Subsequent analysis of the integral data by Abel inversion to obtain local data was carried out so information on the local flow behaviour in the frequency domain was received. In the case of strong acoustic waves, real and imaginary parts of the signal had to be taken into account when Abel inversion was performed, otherwise signal magnitude can be used for inversion. Quantitative comparison of some local density fluctuation profiles (received from the interferometric data by Abel inversion) to local data recorded with CTA or pressure sensors showed certain similarities in cases where the SNR of the optical phase fluctuations detected by the velocity decoder was sufficient and where averaging of the light wave on a large number of uncorrelated structures was taken into account. Besides the measurement of turbulent structures in compressible flows, this technique can easily provide trigger signals for measurements in periodic flows by filtering in the frequency domain – similar to the well-known procedures in vibration analysis of solid objects. In the case of compressible fluids these might be wakes or boundary-layer separation which can then be detected in a non-intrusive way, e.g. by laser Doppler velocimetry (Mayrhofer et al. 2000) or particle image velocimetry. Also, the sensitivity against pressure waves could be most useful when noise production in turbulent flows is investigated. This technique appears to provide additional information especially in high speed compressible flows or flows at raised temperatures, when otherwise data are difficult to obtain by intrusive methods.

References

Backus GE; Gilbert F (1970) Uniqueness in the inversion of inaccurate gross earth data. Phil Trans R Soc London A 266: 123–192

Brown GM; Forbes JW; Marchi MM; Wales RR (1999) Hologram interferometry in automotive component vibration testing. In: Jüptner WPO; Patorski K (eds) Interferometry '99. SPIE Proc Series, vol 3745, pp 146–152

Edwards RV (1994) Processing of random data. In: Lading L; Wigley G; Buchhave P (eds) Optical diagnostics for flow processes. Plenum Press, New York, pp 69–84

Garg S; Settles GS (1998) Measurements of a supersonic turbulent boundary layer by focusing Schlieren deflectometry. Exp Fluids 25: 254–264

Gostelow JP; Melawani N; Walker GJ (1996) Effects of streamwise pressure gradient on turbulent spot development. J Turbomach 118: 737–743

Gostelow JP; Walker GJ; Solomon WJ; Hong G; Melwani N (1997) Investigation of the calmed region behind a turbulent spot. J Turbomach 119: 802–809

Heinemann H-J; Lawaczeck O; Bütefisch KA (1976) Karman vortices and their frequency determination in the wakes of profiles in the sub- and transonic regime. In: Oswatitsch K; Rues D (eds) Symposium. Transonicum II, Göttingen, International Union of Theoretical and Applied Mechanics. Springer, Berlin Heidelberg New York

Hipp M; Reiterer P; Woisetschläger J; Philipp H; Pretzler G; Fliesser W; Neger T (1999) Application of interferometric fringe evaluation software at Technical University Graz. In: Jüptner WPO; Patorski K (eds) Interferometry '99. SPIE Proc Series, vol 3745, pp 281–292

Kreis T (1996) Holographic interferometry. Akademie, Berlin

Lewin AC; Mohr F; Selbach H (1990) Heterodyn-Interferometer zur Vibrationsanalyse. Technisches Messen 57(9): 335–345

Lewin A (1999) New compact laser vibrometer for industrial and medical applications. In: Tomasini EP (ed) Third International Conference on Vibration Measurements by Laser Techniques, SPIE Proc Series, vol 3411, pp 61–67

Mayle RE (1991) The role of laminar–turbulent transition in gas turbine engines. J Turbomach 113: 509–537

Mayle RE; Dullenkopf K; Schulz A (1998) The turbulence that matters. J Turbomach 120: 402–409

Mayrhofer N; Lang H; Woisetschläger J (2000) Experimental investigation of turbine wake flow by interferometrically triggered LDV-measurements. 10th International Symposium on Application of Laser Techniques to Fluid Mechanics, Instituto Superior Tecnico, Lisboa, Paper 28-1

McComb WD (1990) The physics of fluid turbulence, Oxford Engineering Science Series 25. Oxford University Press, Oxford

Merzkirch W (1987) Flow visualization. Academic Press, Orlando

Newland DE (1975) Random vibrations and spectral analysis. Longman, London

Oertel H sen; Oertel H jun (1989) Optische Strömungsmeßtechnik. G Braun, Karlsruhe

Pretzler G; Jäger H; Neger T; Philipp H; Woisetschläger J (1992) Comparison of different methods of Abel-inversion using computer simulated and experimental side-on data. Z Naturforsch 47a: 955–970

Randall RB; Tech B (1977) Application of B & K equipment to frequency analysis. Bruel & Kjaer, Naerum, Denmark

Romano GP (1995) Analysis of two-point velocity measurements in near wall flows. Exp Fluids 20: 68–83

Selbach H; Lewin AC; Roth V (1992) Laser Doppler vibrometer for applications in the automotive industry. 25th International Symposium on Automotive Technology and Automation, Florence. Fraunhofer Institut, Aachen

Vest CM (1989) Holographic interferometry. Wiley, New York

Vukičević D; Neger T; Jäger H; Woisetschläger J; Philipp H (1990) Optical tomography by heterodyne holographic interferometry. SPIE Institute Series, vol 8, pp 160–193